

# Understanding the Ion-Sorption Dynamics in Functionalized Porous Carbons for Enhanced Capacitive Energy Storage

Hai Su, Haichao Huang, Shenlong Zhao, Yihao Zhou, Shumao Xu, Hong Pan, Bingni Gu, Xiang Chu, Wen Deng, Hepeng Zhang, Haitao Zhang,\* Jun Chen,\* and Weiqing Yang\*



Cite This: *ACS Appl. Mater. Interfaces* 2020, 12, 2773–2782



Read Online

ACCESS |



Metrics & More



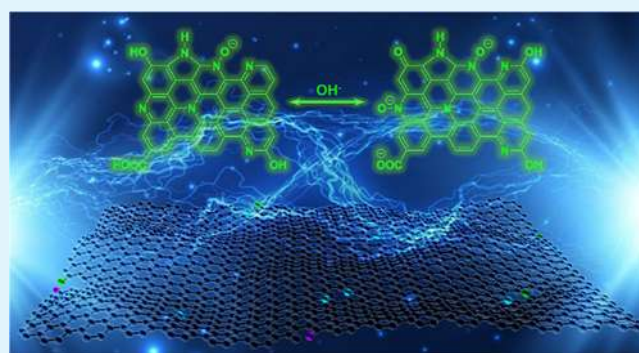
Article Recommendations



Supporting Information

**ABSTRACT:** Heteroatom-functionalized porous carbon has long been regarded as a promising electrode material to construct high-performance capacitive energy storage devices. However, the development of this field is seriously limited due to the lack of an in-depth understanding of the ion-sorption dynamics. Herein, the component and structure controllable N, O, and Cl codoped bimodal (micro-to-meso) porous carbons were prepared and further used as the investigated object for exploring the intrinsic ion-sorption dynamics, which is the root of the enhanced electrochemical response in capacitive energy storage devices. Voltammetry response analysis is employed to quantify the charge storage contributions from both electrostatic adsorption effect (electrical double-layer capacitance) and highly reversible redox process (pseudocapacitance). The existence of electronic capacitance enables a positive correlation between surface capacitance and the ratio of micropores. Besides, an electron-dependent correlation between the electroactive functional groups and redox reaction induced capacitance is also explored. This work will advance the capacitive energy storage field by presenting a clear understanding of the ion-sorption dynamics in the functionalized porous carbons.

**KEYWORDS:** ion-sorption dynamics, pore structure, heteroatom doping, double-layer capacitance, pseudocapacitance



## INTRODUCTION

With the threats of global warming and energy crisis, searching for clean and renewable energy sources, as well as new technologies for efficient energy conversion and storage, is one of the most urgent challenges to the sustainable development of human civilization.<sup>1–10</sup> Batteries,<sup>11–13</sup> fuel cells,<sup>14–16</sup> and supercapacitors<sup>17–19</sup> are the most effective and practical technologies for electrochemical energy conversion and storage. Among them, supercapacitors have attracted significant attentions due to their high power density, long lifecycle, and combining advantages from both traditional dielectric capacitors (high power output) and batteries/fuel cells (high energy output).<sup>20–26</sup> To build up a high-performance supercapacitor, increasing the electrode specific surface area (SSA),<sup>27,28</sup> designing its pore structure,<sup>29–31</sup> improving its electrical conductivity,<sup>32,33</sup> and surface heteroatom doping<sup>34,35</sup> are the widely recognized routines to modify the electrodes for capacitive energy storage. Although substantial progress had been achieved recently, the related enhancement mechanism and effect of intrinsic ion-sorption dynamics on capacitive performance, namely, the electric double-layer capacitance (EDLC) enabled by the surface electrostatic adsorption effect and pseudocapacitive performance, that is, the highly reversible redox reaction contributed pseudocapacitance in heteroatom-

functionalized porous carbons are still unclear, which are the keys to designing high-performance electrode materials and advancing the field of capacitive energy storage.

Carbide-derived carbons (CDC), a class of porous carbon materials, possess inherent advantages for both the performance and mechanism study due to their structural characteristics. For example, tunability of the functional groups on the CDC surface allows us to control over the species and contents of the electronegativity elements such as nitrogen,<sup>36–38</sup> oxygen,<sup>39,40</sup> sulfur,<sup>41</sup> and chlorine,<sup>42,43</sup> thereby providing an ideal platform for the in-depth understanding of the related mechanism. Also, the synergistic effect between the unique hierarchical structure and heteroatom doping could not only result in anomalous capacitance increase,<sup>29,44</sup> but also further improve the capacitance by enhancing electropolarity and electron density in carbon lattice, and bringing in redox reactions.<sup>45–47</sup> However, combining hierarchical pores and heteroatom doping encounters multistep processing and

**Received:** September 1, 2019

**Accepted:** December 23, 2019

**Published:** December 23, 2019



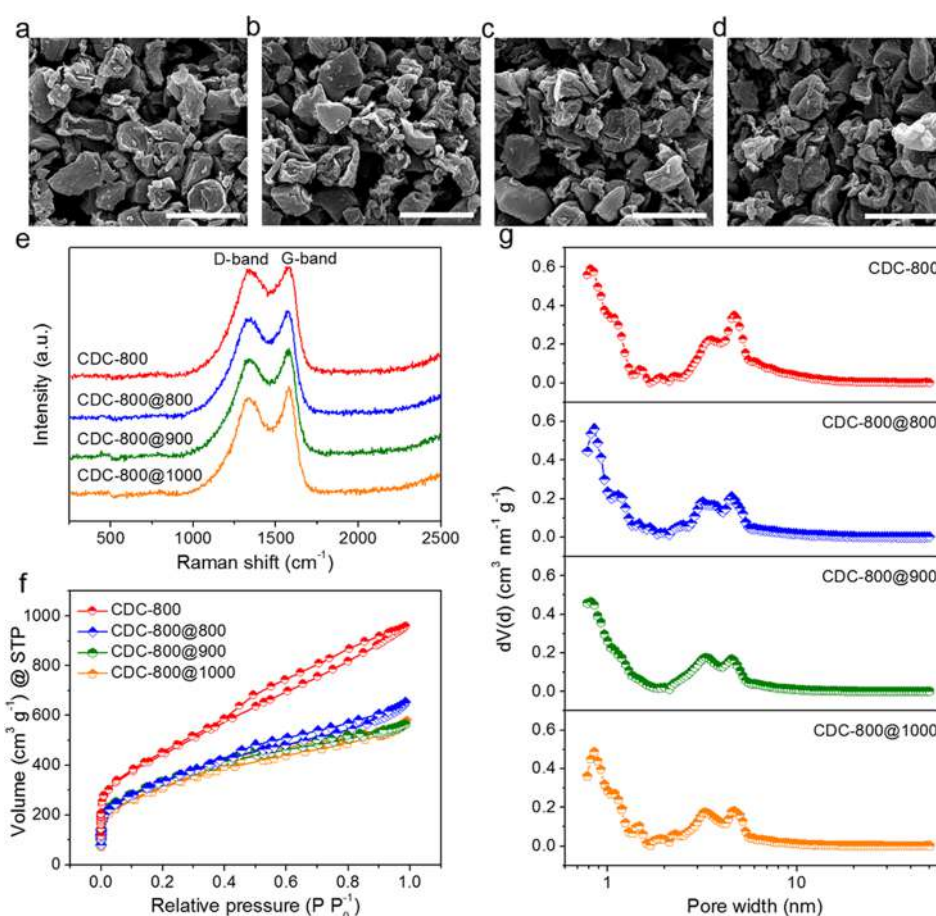


**Figure 1.** Micromorphological and microstructural characterizations of the CDCs. SEM images of the (a) CDC-800, (b) CDC-800@800, (c) CDC-800@900, and (d) CDC-800@1000. The scale bars are 5  $\mu\text{m}$ . (e) Raman spectra. (f) Nitrogen adsorption/desorption isotherms. (g) Corresponding PSD curves calculated by the DFT method.

undesirable electrochemical performance.<sup>48–50</sup> Therefore, exploring a simple and effective method to design desirable CDC materials with a controllable component and microstructure to understand the ion-sorption dynamics in capacitive energy storage devices is highly desired.

Herein, to explore the underlying reasons for the enhanced capacitive energy storage capacity enabled by heteroatom-functionalized porous carbons, a N, O, and Cl codoped CDC was prepared through chlorination of  $\text{TiC}_{0.5}\text{N}_{0.5}$  and employed as the research target. The microstructures and surface elements of the products were further tailored by employing a post-annealing process. Toward giving an insight into the intrinsic ion-sorption dynamics, the electrochemical impedance spectra were analyzed, and the convex mesostructures as well as the heteroatom-doped depressed ion-sorption dynamics with prolonged relaxation time were confirmed. The separate capacitance contributions from the surface physisorption effect, namely, EDLC, and heteroatom-inductive redox process, namely, pseudocapacitance, were quantified fundamentally based on the dynamic voltammetry response analysis. In depth, the relationship between surface EDLC enabled by the porous microstructures and the ratio of micropores was established, indicating the positive correlation due to the induced electronic capacitance from pore size dependent electrolyte ion adsorption for porous carbon materials with submicropores. Furthermore, the exhaustive pseudocapacitance contributions from respective electrochemical active

functional groups in alkaline electrolyte based on the electron transfer number during the redox process were disclosed, which demonstrates the availability by designing the heteroatom bonding style to achieve the enhanced capacitive performance. This work shed light on the effect of the ion-sorption dynamics on capacitive performance in functionalized porous carbons and enabling further advances in the capacitive energy storage devices.

## EXPERIMENTAL SECTION

**Preparation of Nitrogen, Oxygen, and Chlorine Codoped CDCs.** Two grams of  $\text{TiC}_{0.5}\text{N}_{0.5}$  powders (with a particle size of 1.5–3.0  $\mu\text{m}$ ) were spread out on a graphite foil and continuously heated up to 800  $^{\circ}\text{C}$  with a ramp rate of 5  $^{\circ}\text{C min}^{-1}$  under Ar atmosphere, and then, chlorine ( $\text{Cl}_2$ ) as a chemical etching agent was infused to extract Ti atoms from the precursor lattice. After holding the temperature at 800  $^{\circ}\text{C}$  for 4 h, the residual species in the obtained samples were removed by replenishing Ar. After 2 h, the reaction chamber was cooled down to room temperature to obtain the carbide-derived carbons, namely, CDC-800. The as-prepared CDC-800 went through post-annealing treatment at 800, 900, and 1000  $^{\circ}\text{C}$  for 2 h to obtain the samples CDC-800@800, CDC-800@900, and CDC-800@1000, respectively.

**Characterization of Materials.** The morphologies of the as-prepared CDC materials were characterized by a JEOL JSM-7800 scanning electron microscope (SEM) and JEOL JEM-2100 transmission electron microscope (TEM). X-ray diffraction (XRD) patterns were recorded on a PANalytical X'Pert powder diffractometer using  $\text{Cu K}\alpha$  as the radiation source and a scan range

between 5° and 80°. To analyze the surface chemical composition and the chemical bonding status, X-ray photoelectron spectroscopy (XPS) measurements were performed on a Thermo Scientific ESCALAB 250Xi apparatus with Al K $\alpha$  radiation. Raman spectra were conducted on a RM2000 microscopic confocal Raman spectrometer with a laser wavelength of 532 nm. Nitrogen adsorption/desorption characterization was used to determine the SSA and porosity at 77 K with a Quantachrome 2SI-MP-9 surface area and pore size analyzer. Before the measurement, all samples were outgassed at 150 °C under vacuum for 12 h to remove the adsorbed air gas.

**Preparation of CDC Electrodes.** To prepare CDC electrodes, CDC powders, acetylene black, and polytetrafluoroethylene (PTFE) dispersion (60 wt%), with a weight ratio of 85:10:5, were mixed together in isopropyl alcohol. After that, the mixture was dried at 80 °C to remove all isopropyl alcohol. The mixture was subsequently rolled into a thin film with a thickness of  $100 \pm 5 \mu\text{m}$ . Finally, the thin film was shaped into an 8 mm diameter disk and pressed onto nickel foam (NF) for measurements, where NF was used as the current collector.

**Electrochemical Characterizations.** The electrochemical performance of CDCs was evaluated in 6 M KOH under the conventional three-electrode configuration using a CHI660E electrochemical workstation. In this system, the prepared CDC electrodes, platinum sheet, and Hg/HgO were used as the working electrode, counter electrode, and reference electrode, respectively. The applied potential window was set between  $-1$  and  $0$  V for cyclic voltammetry (CV) and galvanostatic charge/discharge (GCD) measurements. Electrochemical impedance spectroscopy (EIS) was performed in a frequency range from  $10^5$  to  $10^{-1}$  Hz at a stimulated amplitude of 5 mV.

## RESULTS AND DISCUSSION

### Micromorphologies and Microstructures of the CDCs.

The micromorphologies of the precursor and the as-prepared CDC materials were observed by employing both the SEM and TEM. The obtained SEM and TEM images are shown in Figure 1a–d and Figures S1 and S2. It is noticed that the precursor exhibits blocked-like surface morphology (Figure S1), while the yielding sample exhibited a mixture of both blocked-like and wrinkle-like micromorphologies after precursor chlorination at 800 °C for 4 h (CDC-800) (Figure 1a and Figure S2). It is attributed to the variation of titanium atom chemical etching rates and the mechanisms of reaction between carbonitrides and chlorine. Consequently, the different thermodynamic process can be achieved to generate different structure cracks and shrinks in the derived carbon layers.<sup>51</sup> After post-annealing treatment at different temperatures, the micromorphologies for CDC-800@800, CDC-800@900, and CDC-800@1000 were respectively obtained, as shown in Figure 1b–d. There are no obvious differences between the samples after post-annealing treatment and the pristine ones, which demonstrates that the conformal transformation can effectively avoid the structure disturbance, eliminating the effect from morphological heterogeneity on the ion-sorption dynamics.

XRD, Raman spectra, and nitrogen adsorption/desorption measurements were performed to systematically characterize the internal structure of the CDCs. As shown in the phase composition of CDC-800 (Figure S3), two prominently broad and weak diffraction peaks emerge, which confirmed that the chlorination treatment converted the CDC structure from a cubic lattice to an amorphous and/or short-range ordered structure. Figure 1e shows the Raman spectra for all the CDC materials, in which two distinct peaks emerged at  $\sim 1350$  and  $1580 \text{ cm}^{-1}$ . The former (D-band) indicates the presence of structure defects and disorders, which is related to the

vibrations of carbon atoms with dangling bonds in the plane terminations, while the latter (G-band) is ascribed to the vibrations of  $\text{sp}^2$ -bonded carbon atoms in the honeycomb-like carbon lattice, namely, the stretching modes of C=C bonds, indicating a graphite structure.<sup>52</sup> Clearly, the intensity of the G-band becomes stronger compared to the D-band after post-annealing treatment, which indicates an increase of the degree of the ordered structure in CDC materials. In general, the intensity ratio between D-band and G-band ( $I_{\text{D}}/I_{\text{G}}$ ) was used to quantify the structural differences. Therefore, the Raman spectra were deconvoluted for all the samples. To improve the accuracy, Raman spectra were recorded at four different regions for each sample, and the curves were fitted using four ancillary bands (Figures S4 to S7). The values of  $I_{\text{D}}/I_{\text{G}}$  can be obtained by using the accumulated peak areas. According to Table S1, the values of  $I_{\text{D}}/I_{\text{G}}$  are  $2.05 \pm 0.04$ ,  $1.80 \pm 0.12$ ,  $1.77 \pm 0.11$ , and  $1.60 \pm 0.20$  for CDC-800, CDC-800@800, CDC-800@900, and CDC-800@1000, respectively. Furthermore, the effective crystallite size ( $L_c$ ) in the direction of the graphite plane of the four CDCs can also be calculated, with values of  $2.12 \pm 0.04$ ,  $2.43 \pm 0.17$ ,  $2.47 \pm 0.15$ , and  $2.78 \pm 0.38$  nm, respectively. Consequently, the post-annealing treatment can significantly increase the sample crystallinity, resulting in highly ordered structures.

SSA and electrode porosity are also critical to improve the capacitive performance. Nitrogen adsorption/desorption isotherms of the CDC materials were obtained at 77 K, as shown in Figure 1f. Obviously, type I and IV isotherms with hysteresis loops when the  $P/P_0$  is higher than 0.4 are present for all the CDC materials, indicating the presence of micro- and mesopores.<sup>53,54</sup> As presented in Table S2, the value of SSA calculated from the Brunauer–Emmett–Teller (BET) method ( $S_{\text{BET}}$ ) for CDC-800 is  $1580 \text{ m}^2 \text{ g}^{-1}$ , which was decreased after the post-annealing temperatures increased from 800 to 1000 °C due to the pore structure collapse. Interestingly, no observable differences were found for the  $S_{\text{BET}}$  of all the post-annealing treated CDC materials. Similarly, the variation for the value of the SSA derived from the density functional theory (DFT) method ( $S_{\text{DFT}}$ ) is consistent with  $S_{\text{BET}}$ , and the corresponding values are 1405, 1037, 1001, and  $926 \text{ m}^2 \text{ g}^{-1}$  for CDC-800, CDC-800@800, CDC-800@900, and CDC-800@1000, respectively. Furthermore, the DFT pore size distribution (PSD) was evaluated to investigate the porosity of the CDC materials, as shown in Figure 1g. It can be seen that all of the CDC materials possess a hierarchical porous structure with a wide-range of pore sizes from micropores to mesopores. Also, the Barret–Joyner–Halenda (BJH) method was applied to measure the PSD (Figure S8). Almost no macropores can be perceived, which means that the CDC materials are micro- and mesopores. The specific surface area of micropores and mesopores derived from the DFT method is also presented in Table S2. The total pore volume ( $V_t$ ) values are 1.48, 1.01, 0.88, and  $0.90 \text{ cm}^3 \text{ g}^{-1}$  for CDC-800, CDC-800@800, CDC-800@900, and CDC-800@1000, respectively. To measure the volume of micropores and mesopores, the  $t$ -plot was employed to characterize the inner pore properties. CDC-800 owns the highest volume of mesopores ( $V_{\text{meso}}$ ). However, this value was continuously decreasing with the elevated post-annealing temperatures due to the structure evolution of the carbon layer and the removal of unfirmed functional groups at a higher temperature, giving rise to the collapse of partial mesopores and micropores.

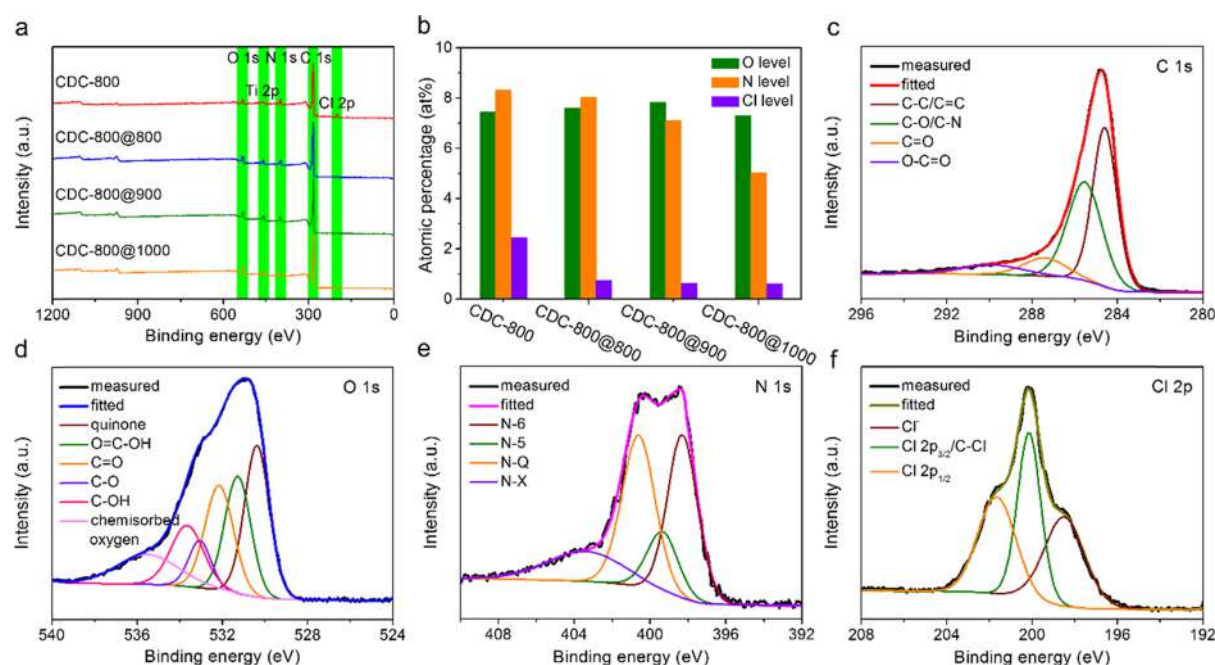


**Figure 2.** Surface composition analysis of the CDCs. (a) XPS survey spectra. (b) O, N, and Cl levels. Deconvoluted high-resolution (c) C 1s, (d) O 1s, (e) N 1s, and (f) Cl 2p XPS spectra.

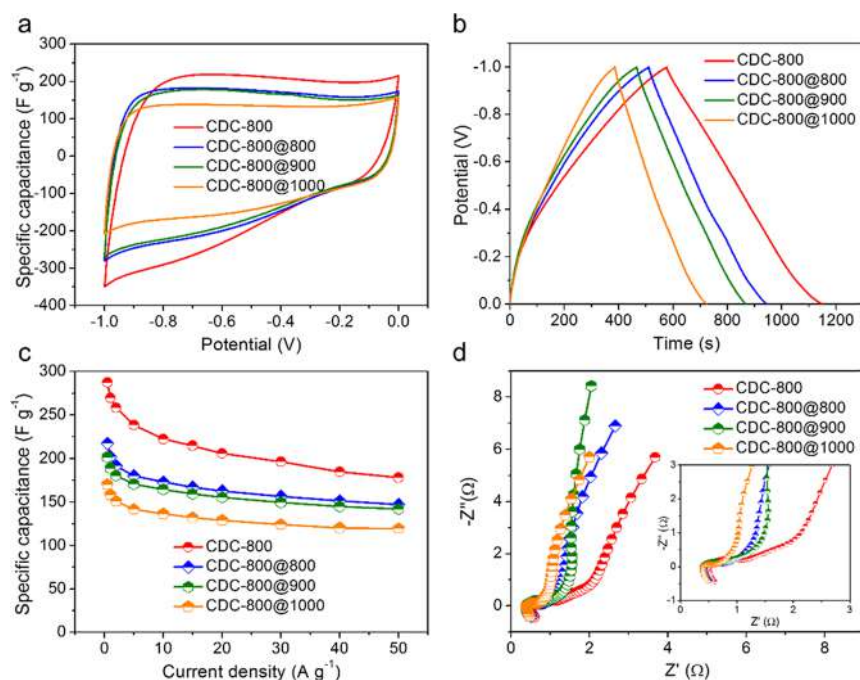


**Figure 3.** Electrochemical performance evaluation of the CDC electrodes in a three-electrode configuration. (a) CV curves at a scan rate of  $50 \text{ mV s}^{-1}$ . (b) GCD curves at a current density of  $0.5 \text{ A g}^{-1}$ . (c) Dependence of the specific capacitance on the current densities. (d) Nyquist plot. The inset presents the zoom-in Nyquist plots in the high-frequency region.

**Elemental Composition and Chemical State of the CDCs.** XPS was applied to analyze the elemental composition and chemical state for the heteroatom-doped carbon materials. As shown in Figure 2a, the XPS survey spectra confirmed the presence of doped C, N, O, and Cl in the CDC materials, which is in accordance with the EDS element mapping results in Figures S9 to S12. A weak Ti 2p peak was also observed, which is attributed to the incomplete removal of the reaction by-products at the input of detergent Ar. Atomic percentages of the N, O, and Cl levels in CDC materials are presented in

Figure 2b. It is obvious that the yielding CDC-800 possesses the highest N and Cl levels. With the increase of the post-annealing temperatures, the contents of N and Cl were decreased from 8.32 to 5.01 at % for the N level and 2.44 to 0.61 at % for the Cl level in the CDC materials. Meanwhile, the contents of the O level for four samples hold almost constant at the elevated post-annealing temperatures, with values of 7.45, 7.61, 7.85, and 7.31 at %. Furthermore, the high-resolution C 1s, N 1s, O 1s, and Cl 2p XPS spectra were deconvoluted to investigate the elemental bonding status

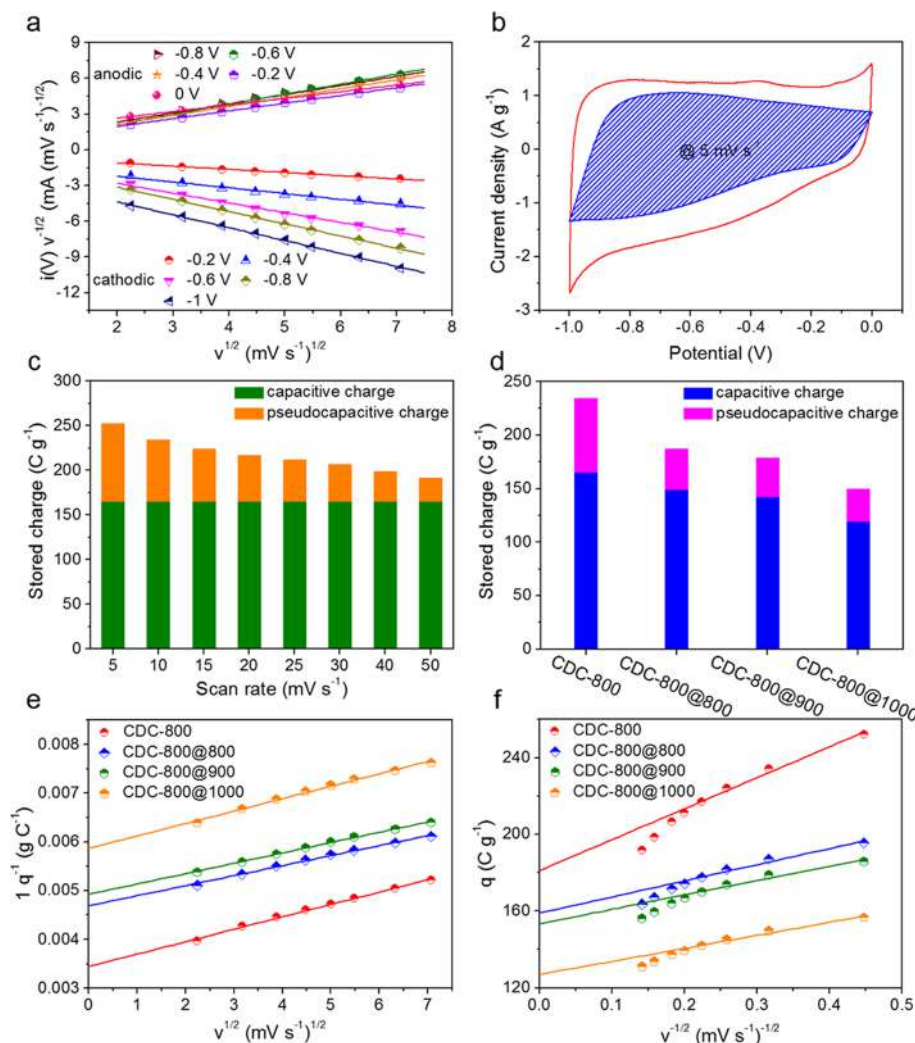


**Figure 4.** Analysis of the capacitance contributions in CDCs. (a) Dependence of voltammetric currents on the scan rates at different potentials for the CDC-800 electrode. (b) Surface capacitive and pseudocapacitive contributions to charge storage between  $-1$  and  $0$  V at a scan rate of  $5 \text{ mV s}^{-1}$ . The surface capacitive contribution to the total measured current is shown as the shaded region for the CDC-800 electrode. (c) Separation of contributions from surface capacitive and pseudocapacitive charges at different scan rates for the CDC-800 electrode. (d) Comparison of the contribution from the surface capacitive effect and faradic redox process to the total stored charge at a scan rate of  $10 \text{ mV s}^{-1}$ . (e) Relationship between the reciprocal voltammetry charge  $1/q$  and the square root of scan rate  $v^{1/2}$ . (f) Voltammetry charge  $q$  versus the reciprocal square root of scan rate  $v^{-1/2}$ .

inside CDCs. As shown in Figure 2c and Figure S13, the fitted high-resolution C 1s XPS spectra demonstrated four component peaks, allocating to C–C/C=C ( $\sim 284.7 \text{ eV}$ ), C–O/C–N ( $\sim 285.8 \text{ eV}$ ), C=O ( $\sim 287.7 \text{ eV}$ ), and O–C=O ( $\sim 289.5 \text{ eV}$ ) groups.<sup>55–57</sup> Furthermore, the high-resolution O 1s XPS spectra of the CDCs are presented in Figure 2d and Figure S14. The oxygen atoms existed in all the CDCs with the form of quinone ( $\sim 530.40 \text{ eV}$ ), carboxyl ( $\sim 531.20 \text{ eV}$ ), carbonyl ( $\sim 532.18 \text{ eV}$ ), C–O ( $\sim 533.05 \text{ eV}$ ), phenol/C–OH ( $\sim 533.70 \text{ eV}$ ), and chemisorbed oxygen ( $\sim 535.50 \text{ eV}$ ).<sup>58,59</sup> Figure 2e and Figure S15 show the high-resolution N 1s XPS spectra, which shows four peaks centering at  $\sim 398.3$ ,  $399.6$ ,  $401.0$ , and  $403.5 \text{ eV}$ , corresponding to pyridine N (N-6), pyridone and/or pyrrolic N (N-5), quaternary and/or graphitic-like N (N-Q), and oxidized pyridine N (N-X), respectively.<sup>60–62</sup> Besides, the obtained high-resolution Cl 2p XPS spectra can be divided into three peaks centered at  $\sim 198.2$ ,  $200.6$ , and  $202.2 \text{ eV}$ , which corresponds to  $\text{Cl}^-$ , Cl  $2p_{3/2}$  and/or C–Cl, and Cl  $2p_{1/2}$  groups, respectively (Figure 2f

and Figure S16).<sup>63,64</sup> In addition, the detailed element and chemical bonding levels are presented in Tables S3 and S4.

**Electrochemical Performance Evaluation of the CDC Electrodes.** To investigate the capacitive properties of the as-prepared CDC materials, CV, GCD curves, and EIS were measured in  $6 \text{ M KOH}$  aqueous electrolyte using a three-electrode configuration, as shown in Figure 3 and Figure S17. Figure 3a is the typical CV curves for the four CDC samples at a scan rate of  $50 \text{ mV s}^{-1}$ . A larger negative current of the cathodic branches was found compared to the anodic branches in the negative potential region, which is attributed to the presence of pseudocapacitance induced by doping strong electronegative heteroatoms into carbon lattices.<sup>65</sup> With the increase of post-treatment temperatures, the CDCs exhibit a smaller enclosed area compared to CDC-800, which revealed the gradually decreasing capacitance due to the reduced SSA and heteroatom contents. Figure 3b depicts the GCD curves at a current density of  $0.5 \text{ A g}^{-1}$ . The dependence of the specific capacitance on the current densities for all CDCs is shown in

Figure 3c. The specific capacitance values at 0.5 A g<sup>-1</sup> are 287.4, 217.4, 201.6, and 170.1 F g<sup>-1</sup> for CDC-800, CDC-800@800, CDC-800@900, and CDC-800@1000, respectively, corresponding to capacitance retention values of 61.9%, 67.7%, 70.2%, and 70.3%, respectively, at a higher load current of up to 50 A g<sup>-1</sup>. CDC-800 possesses the highest specific capacitance in a wide range of current densities, and the values gradually decreased with the increase of the post-annealing temperatures. The higher crystallinity and order degree for CDC-800 render its decent electrical conductivity, which contributed to its lifting rate capability. Figure 3d shows the Nyquist plots; the abscissa axis intercept point evolved equivalent series resistance (ESR) values are 0.52, 0.40, 0.40, and 0.41 Ω for CDC-800, CDC-800@800, CDC-800@900, and CDC-800@1000, respectively. A lower equivalent series resistance is efficient to rapid charge transfer and high power delivery. The charge-transfer resistance ( $R_{ct}$ ) values that correspond to the diameter of a semicircle over a high-frequency region are 0.41, 0.24, 0.24, and 0.21 Ω for CDC-800, CDC-800@800, CDC-800@900, and CDC-800@1000, respectively, and the Warburg resistance can also be analyzed; CDC-800 exhibits the highest ohmic resistance ( $W-R$ ) and time content ( $W-T$ ), suggesting the sluggish dynamics due to the involvement of the inferior redox process (i.e., pseudocapacitance). Toward giving an insight into the inherent dynamics further, Bode phase angle plots are presented in Figure S18. Based on the developed theory by Kant and Singh,<sup>66</sup> the mesoscale morphological structure influences the diffuse layer dynamics for a porous electrode consisting of arbitrary-shaped mesostructures with embedded cylindrical micropores. It can be seen that all of the measured electrodes showed smooth plots, not a hump, in the high-frequency region, indicating that the mesostructure is convex for our CDC materials. The combined effects of geometry and the size of EDL enable the easy access and fast reorganization for EDL. In a low-frequency range, the effect of heteroatoms that contributed to the pseudocapacitance is very strong, which is implied by the dramatically decreasing phase angle of CDC-800 (only -57.2°) compared to the other three samples (about 68.9–76.3°). In a relatively high-frequency range, an apparent relaxation peak occurs for all the samples, however, the relaxation time gradually decreases from CDC-800 (3.92 s) to CDC-800@800 (1.56 s), CDC-800@900 (1.37 s), and further to CDC-800@1000 (1.29 s). This positive transition means that the electrochemical response is optimized after high-temperature treatment for CDC samples, indicating the improved ion-sorption dynamics. For comparison, the electrochemical performance of the commercially activated carbon (AC, YP-50F) was also measured under identical electrochemical parameters (Figure S19). Clearly, the AC electrode possesses undesirable specific capacitance and rate capability, which is mainly attributed to the unsuitable pore size for electrolyte ion transportation and EDL establishment (Figure S20).

#### Differentiation of the Charge Storage Contributions.

The influence of the hierarchical porous structure incorporation with heteroatom doping on charge storage needs to be explored in-depth for understanding the kinetic process at supercapacitor charge/discharge status. Furthermore, a voltammetry response analysis technique was employed to quantify the capacitance contributions from nonfaradic process-induced electric double-layer capacitance and faradic redox reaction-evolved pseudocapacitance from heteroatom

doping. The measured current at fixed potential can be separated into the capacitive current ( $k_1v$ ) and diffusion-controlled current ( $k_2v^{1/2}$ )<sup>67,68</sup> as shown in the equation

$$i(V) = k_1v + k_2v^{1/2}, \text{ where } k_1 \text{ and } k_2 \text{ are numerical constants.}$$

To differentiate the capacitive contributions, we first determined the  $k_1$  value at fixed potential by plotting the linear relation between  $i(V)/v^{1/2}$  and  $v^{1/2}$  at various scan rates (5–50 mV s<sup>-1</sup>), as shown in Figure 4a. These values of  $k_1$  at different potentials can be determined as their slopes. Numerous  $k_1v$  values, depending on the potentials at a fixed scan rate, could form an enclosed CV curve to estimate the stored charges. Herein, the partial contribution from the capacitive current can be calculated as the area of shaded regions. Figure 4b presents the CV curve and current response–potential plot of the capacitance contribution at a scan rate of 5 mV s<sup>-1</sup> for the CDC-800 electrode, and a similar voltammetry response at a higher scan rate of 50 mV s<sup>-1</sup> is presented in Figure S21. Figure 4c compares the stored charges contributed from the surface EDL effect and the faradic redox reaction. Evidently, the stored charge induced by the surface EDL keeps constant at various scan rates, while the stored charge from the faradic redox reaction process exhibits a significantly different trend. The much slower reaction kinetics is responsible for the gradually reduced charge quantity with the increased scan rates, which can be understood that the long relaxation time impedes the faradic charge storage at higher scan rates. The effect of post-annealing treatment for CDC-800 on the capacitance contribution was also investigated. In Figure 4d, the capacitance charges at a scan rate of 10 mV s<sup>-1</sup> from the surface EDL effect are 165.3, 149.1, 142.6 and 119.4 C g<sup>-1</sup>, which are ascribed to the decreased effective SSA and deteriorated pore structure, and the corresponding pseudocapacitance charges are 69.1, 38.1, 36.1 and 30.3 C g<sup>-1</sup>, respectively, induced by the oxygen- and nitrogen-containing groups (namely, carboxyl, phenol, and N-6).

Furthermore, the capacitance contributions from surface EDL and faradic redox reactions can be also differentiated.<sup>69,70</sup> In this procedure, the voltammetry charge ( $q$ ) was calculated at different scan rates, and the scatter diagram of  $1/q$  versus  $v^{1/2}$  and  $q$  versus  $v^{-1/2}$  can be plotted subsequently. To obtain the total voltammetry charge ( $q_t$ ), extrapolating of  $q$  to  $v = 0$  from the plot of  $1/q$  versus  $v^{1/2}$  was conducted (Figure 4e). The charge from double layer ( $q_{dl}$ ) is evaluated by extrapolating of  $q$  to  $v = \infty$  from the plot of  $q$  versus  $v^{-1/2}$  (Figure 4f). Consequently, the charge contributed by pseudocapacitance involving faradic redox reactions ( $q_p$ ) can be obtained from the difference between  $q_t$  and  $q_{dl}$ . Furthermore, the specific capacitance (including maximum total specific capacitance ( $C_t$ ), specific electric double-layer capacitance ( $C_{dl}$ ), and specific pseudocapacitance ( $C_p$ )) can be calculated by dividing the corresponding charge within the applied potential windows in CV measurements. Owing to the higher effective O- and N-containing groups, 108.8 C g<sup>-1</sup> is the charge contributed from pseudocapacitance for CDC-800, and the values are 54.3, 49.4, and 43.4 C g<sup>-1</sup> for CDC-800@800, CDC-800@900, and CDC-800@1000, respectively. More detailed results are listed in Table S4.

**The Root of EDL Capacitance and Pseudocapacitance.** To further understand the capacitance contributions either from the surface effect dedicated to EDL capacitance or active functional group-induced pseudocapacitance, the variation of the surface capacitance ( $C_{surf}$ ) with the ratio of the micropore surface area ( $R_{micro}$ ) is shown in Figure Sa.

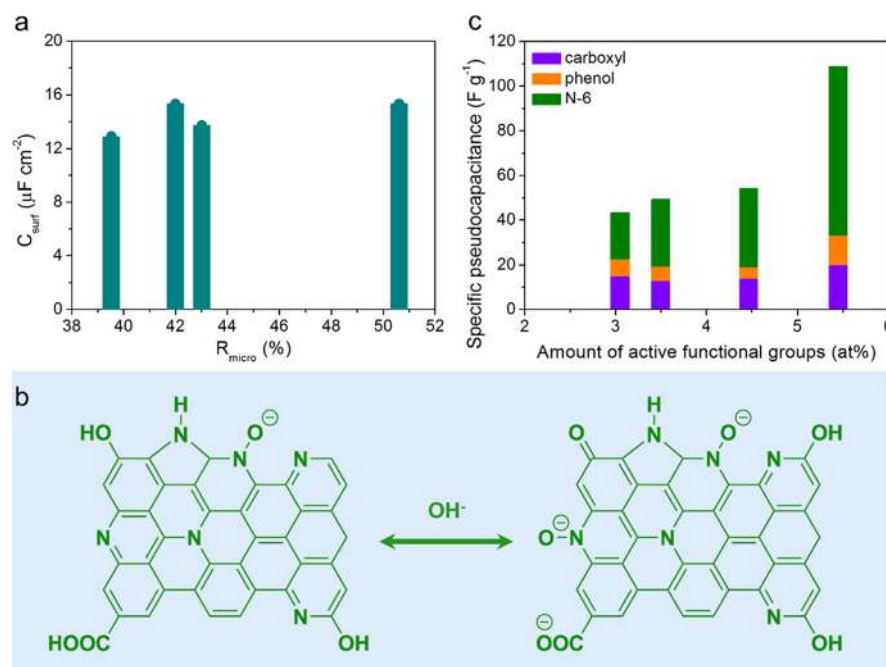


**Figure 5.** Quantification the contribution of the surface effect and functional groups to the subdivided capacitance. (a) Dependence of the specific surface area normalized capacitance on the ratio of the micropore surface area. (b) Redox reactions for N- and O-doped electrode materials in alkaline electrolytes. (c) Portion of the pseudocapacitance contributing from different active functional groups.

Meaningfully, a variation of the steady increase of the values of  $C_{\text{surf}}$  along with the increased micropore amounts can be observed. It is mainly attributed to the existence of electronic capacitance in the subnanoporous carbon materials according to the theory proposed by Kant and Singh.<sup>71</sup>

Furthermore, we quantified the specific pseudocapacitance derived from active oxygen- and nitrogen-containing functional groups. Here, we assumed that the pseudocapacitance was entirely introduced by active oxygen- and nitrogen-containing functional groups due to the negligible capacitance contributions from chlorine-containing functional groups in alkaline electrolytes. Acidic carboxyl and phenol in oxygen-containing functional groups can introduce pseudocapacitance via reacting with hydroxyl ions ( $\text{OH}^-$ ) in the alkaline aqueous electrolyte. Meanwhile, for the nitrogen-containing functional group, the redox reactions occurred between N-6 and pyridone and/or between N-6 and N-X. The involved electron transfer reactions are presented in Figure 5b and Note S1.

Based on the involved redox equations, the respective specific pseudocapacitance versus the amount of active functional groups (including carboxyl, phenol, and N-6) is shown in Figure 5c, and a detailed calculation method is demonstrated in Note S2. It is shown that the CDC-800 electrode possesses the maximum total specific pseudocapacitance. It is because two electrons are transferred to one N-6 group during the redox reaction process, while only one electron involves for each carboxyl or phenol group, and CDC-800 possesses the highest N-6 groups and similar oxygen content compared to the others. It is also observed that it is not a linear relation between the generated specific pseudocapacitance and corresponding individual atomic percentage. The pseudocapacitance is also related to the effective surface area, which is critical to redox reactions. As a result, a higher effective surface area, suitable pore structure, and higher ratio of active functional groups are the key factors

to achieve the excellent capacitive energy storage performance for heteroatom-doped carbon materials.

## CONCLUSIONS

In summary, the underlying ion-sorption dynamics were explored for the enhanced capacitive performance in heteroatom-functionalized porous carbon materials, combining electrochemical response analysis and establishing the charge storage contributions from a porous structure enabled surface capacitive charge and heteroatom doping contributed pseudocapacitive charge, in which composition and porosity tunable N, O, and Cl codoped CDC materials were used as the research objects. Bode phase angle plots analysis demonstrated the bimodal (micro-to-meso) CDC materials with a convex mesostructure, which favors the accessibility of electrolyte ions and the dynamics of electrolyte ion reorganization for EDL. Besides, heteroatom doping would depress the ion-sorption dynamics due to the sluggish redox reaction process and thus deteriorating the rate capability. The positive correlation between the surface capacitance and the ratio of micropores indicates the existence of electronic capacitance that is relative to pore size dependent ion-sorption dynamics. Furthermore, electroactive pyridine N, carboxyl, and phenol functional groups can induce reversible redox reaction to offer pseudocapacitance in an alkaline aqueous electrolyte, and the pyridine N functional group with more transfer electron numbers during the redox process dominates the contributed pseudocapacitance. Therefore, bimodal porous carbon materials with a convex mesostructure and optimized chemical bonding style to improve the capacitive performance are accessible. This work renders a clear understanding of the roles of EDL and pseudocapacitance in the contribution to an improved capacitance and how to manipulate the two to design high-performance capacitive energy storage devices.

## ■ ASSOCIATED CONTENT

### Supporting Information

The Supporting Information is available free of charge at <https://pubs.acs.org/doi/10.1021/acsami.9b15781>.

XRD patterns of CDC-800 and  $\text{TiC}_{0.5}\text{N}_{0.5}$ ; Raman spectra; PSD curves calculated from the BJH method; structural parameters; high-resolution C 1s, O 1s, N 1s, and Cl 2p XPS spectra for CDC-800@800, CDC-800@900, and CDC-800@1000, and the detailed elemental composition and chemical bonding; CV curves for CDCs with a three-electrode configuration; capacitive and pseudocapacitive contributions to charge storage at a scan rate of  $50 \text{ mV s}^{-1}$ ; capacitance contributions for CDC electrodes from the plot of  $q$  vs  $v^{-1/2}$  and  $1/q$  vs  $v^{1/2}$ ; reaction mechanism in alkaline electrolyte for N- and O-doped carbon materials; and the calculation method for the respective specific pseudocapacitance vs the amount of active functional groups (PDF)

## ■ AUTHOR INFORMATION

### Corresponding Authors

**Haitao Zhang** – Southwest Jiaotong University, Chengdu, China; Email: [haitaozhang@swjtu.edu.cn](mailto:haitaozhang@swjtu.edu.cn)

**Jun Chen** – University of California, Los Angeles, Los Angeles, California; [orcid.org/0000-0002-3439-0495](https://orcid.org/0000-0002-3439-0495); Email: [jun.chen@ucla.edu](mailto:jun.chen@ucla.edu)

**Weiqing Yang** – Southwest Jiaotong University, Chengdu, China; [orcid.org/0000-0001-8828-9862](https://orcid.org/0000-0001-8828-9862); Email: [wqyang@swjtu.edu.cn](mailto:wqyang@swjtu.edu.cn)

### Other Authors

**Hai Su** – Southwest Jiaotong University, Chengdu, China

**Haichao Huang** – Southwest Jiaotong University, Chengdu, China

**Shenlong Zhao** – University of California, Los Angeles, Los Angeles, California

**Yihao Zhou** – University of California, Los Angeles, Los Angeles, California

**Shumao Xu** – University of California, Los Angeles, Los Angeles, California

**Hong Pan** – University of Electronic Science and Technology of China, Chengdu, China

**Bingni Gu** – Southwest Jiaotong University, Chengdu, China

**Xiang Chu** – Southwest Jiaotong University, Chengdu, China

**Wen Deng** – Southwest Jiaotong University, Chengdu, China

**Hepeng Zhang** – Southwest Jiaotong University, Chengdu, China

Complete contact information is available at: <https://pubs.acs.org/doi/10.1021/acsami.9b15781>

### Notes

The authors declare no competing financial interest.

## ■ ACKNOWLEDGMENTS

W.Y., J.C., and H.Z. supervised and guided the whole project. J.C. submitted the manuscript and was the lead contact. W.Y.

and H.Z. thank the financial support from the National Natural Science Foundation of China (no. 51602265), the Special Funding of China Postdoctoral Science Foundation (no. 2018 T110992), and the Sichuan Science and Technology Program (no. 2018RZ0074). J.C. acknowledged the Henry Samueli School of Engineering & Applied Science and the Department of Bioengineering at the University of California, Los Angeles for the startup support.

## ■ REFERENCES

- (1) Wang, Z. L.; Song, J. Piezoelectric Nanogenerators Based on Zinc Oxide Nanowire Arrays. *Science* **2006**, *312*, 242–246.
- (2) Wang, X.; Song, J.; Liu, J.; Wang, Z. L. Direct-Current Nanogenerator Driven by Ultrasonic Waves. *Science* **2007**, *316*, 102–105.
- (3) Chen, J.; Wang, Z. L. Reviving Vibration Energy Harvesting and Self-Powered Sensing by a Triboelectric Nanogenerator. *Joule* **2017**, *1*, 480–521.
- (4) Zhu, G.; Chen, J.; Zhang, T.; Jing, Q.; Wang, Z. L. Radial-Arrayed Rotary Electrification for High Performance Triboelectric Generator. *Nat. Commun.* **2014**, *5*, 3426.
- (5) Yan, C.; Gao, Y.; Zhao, S.; Zhang, S.; Zhou, Y.; Deng, W.; Li, Z.; Jiang, G.; Jin, L.; Tian, G.; Yang, T.; Chu, X.; Xiong, D.; Wang, Z.; Li, Y.; Yang, W.; Chen, J. A Linear-to-Rotary Hybrid Nanogenerator for High-Performance Wearable Biomechanical Energy Harvesting. *Nano Energy* **2020**, *67*, 104235.
- (6) Meng, K.; Zhao, S.; Zhou, Y.; Wu, Y.; Zhang, S.; He, Q.; Wang, X.; Zhou, Z.; Fan, W.; Tan, X.; Yang, J.; Chen, J. A Wireless Textile-Based Sensor System for Self-Powered Personalized Health Care. *Matter* **2020**, *1*, 2637.
- (7) Chen, J.; Huang, Y.; Zhang, N.; Zou, H.; Liu, R.; Tao, C.; Fan, X.; Wang, Z. L. Micro-Cable Structured Textile for Simultaneously Harvesting Solar and Mechanical Energy. *Nat. Energy* **2016**, *1*, 16138.
- (8) Chu, S.; Cui, Y.; Liu, N. The Path Towards Sustainable Energy. *Nat. Mater.* **2017**, *16*, 16–22.
- (9) Zhang, N.; Chen, J.; Huang, Y.; Guo, W.; Yang, J.; Du, J.; Fan, X.; Tao, C. A Wearable All-Solid Photovoltaic Textile. *Adv. Mater.* **2016**, *28*, 263–269.
- (10) Chen, J.; Zhu, G.; Yang, W.; Jing, Q.; Bai, P.; Yang, Y.; Hou, T.-C.; Wang, Z. L. Harmonic-Resonator-Based Triboelectric Nanogenerator as a Sustainable Power Source and a Self-Powered Active Vibration Sensor. *Adv. Mater.* **2013**, *25*, 6094–6099.
- (11) Chen, W.; Li, G.; Pei, A.; Li, Y.; Liao, L.; Wang, H.; Wan, J.; Liang, Z.; Chen, G.; Zhang, H.; Wang, J.; Cui, Y. A Manganese-Hydrogen Battery with Potential for Grid-Scale Energy Storage. *Nat. Energy* **2018**, *3*, 428–435.
- (12) Lee, M.; Hong, J.; Lopez, J.; Sun, Y.; Feng, D.; Lim, K.; Chueh, W. C.; Toney, M. F.; Cui, Y.; Bao, Z. High-Performance Sodium-Organic Battery by Realizing Four-Sodium Storage in Disodium Rhodizonate. *Nat. Energy* **2017**, *2*, 861–868.
- (13) Liu, K.; Kong, B.; Liu, W.; Sun, Y.; Song, M.-S.; Chen, J.; Liu, Y.; Lin, D.; Pei, A.; Cui, Y. Stretchable Lithium Metal Anode with Improved Mechanical and Electrochemical Cycling Stability. *Joule* **2018**, *2*, 1857–1865.
- (14) Duan, C.; Kee, R. J.; Zhu, H.; Karakaya, C.; Chen, Y.; Ricote, S.; Jarry, A.; Cruclin, E. J.; Hook, D.; Braun, R.; Sullivan, N. P.; O'Hayre, R. Highly Durable, Coking and Sulfur Tolerant, Fuel-Flexible Protonic Ceramic Fuel Cells. *Nature* **2018**, *557*, 217–222.
- (15) Stephens, I. E. L.; Rossmeisl, J.; Chorkendorff, I. Toward Sustainable Fuel Cells. *Science* **2016**, *354*, 1378–1379.
- (16) Wang, H.; Abruña, H. D. IrPdRu/C as  $\text{H}_2$  Oxidation Catalysts for Alkaline Fuel Cells. *J. Am. Chem. Soc.* **2017**, *139*, 6807–6810.
- (17) Simon, P.; Gogotsi, Y. Materials for Electrochemical Capacitors. *Nat. Mater.* **2008**, *7*, 845–854.
- (18) Liu, L.; Niu, Z.; Chen, J. Unconventional Supercapacitors from Nanocarbon-Based Electrode Materials to Device Configurations. *Chem. Soc. Rev.* **2016**, *45*, 4340–4363.



- (19) Beidaghi, M.; Gogotsi, Y. Capacitive Energy Storage in Micro-Scale Devices: Recent Advances in Design and Fabrication of Micro-Supercapacitors. *Energy Environ. Sci.* **2014**, *7*, 867–884.
- (20) Winter, M.; Brodd, R. J. What are Batteries, Fuel Cells, and Supercapacitors? *Chem. Rev.* **2004**, *104*, 4245–4270.
- (21) Huang, P.; Lethien, C.; Pinaud, S.; Brousse, K.; Laloo, R.; Turq, V.; Respaud, M.; Demortière, A.; Daffos, B.; Taberna, P. L.; Chaudret, B.; Gogotsi, Y.; Simon, P. On-Chip and Freestanding Elastic Carbon Films for Micro-Supercapacitors. *Science* **2016**, *351*, 691–695.
- (22) Wang, Z.; Su, H.; Liu, F.; Chu, X.; Yan, C.; Gu, B.; Huang, H.; Yang, T.; Chen, N.; Han, Y.; Deng, W.; Zhang, H.; Yang, W. Establishing Highly-Efficient Surface Faradaic Reaction in Flower-Like NiCo<sub>2</sub>O<sub>4</sub> Nano-/Micro-Structures for Next-Generation Supercapacitors. *Electrochim. Acta* **2019**, *307*, 302–309.
- (23) Peng, Y.-Y.; Akuzum, B.; Kurra, N.; Zhao, M.-Q.; Alhabeab, M.; Anasori, B.; Kumbur, E. C.; Alshareef, H. N.; Ger, M.-D.; Gogotsi, Y. All-MXene (2D Titanium Carbide) Solid-State Microsupercapacitors for On-Chip Energy Storage. *Energy Environ. Sci.* **2016**, *9*, 2847–2854.
- (24) Wang, Y.; Song, Y.; Xia, Y. Electrochemical Capacitors: Mechanism, Materials, Systems, Characterization and Applications. *Chem. Soc. Rev.* **2016**, *45*, 5925–5950.
- (25) Wang, Z.; Chu, X.; Xu, Z.; Su, H.; Yan, C.; Liu, F.; Gu, B.; Huang, H.; Xiong, D.; Zhang, H.; Deng, W.; Zhang, H.; Yang, W. Extremely Low Self-Discharge Solid-State Supercapacitors via the Confinement Effect of Ion Transfer. *J. Mater. Chem. A* **2019**, *7*, 8633–8640.
- (26) Chen, L.-F.; Lu, Y.; Yu, L.; Lou, X. W. Designed Formation of Hollow Particle-Based Nitrogen-Doped Carbon Nanofibers for High-Performance Supercapacitors. *Energy Environ. Sci.* **2017**, *10*, 1777–1783.
- (27) Zhu, Y.; Murali, S.; Stoller, M. D.; Ganesh, K. J.; Cai, W.; Ferreira, P. J.; Pirkle, A.; Wallace, R. M.; Cychosz, K. A.; Thommes, M.; Su, D.; Stach, E. A.; Ruoff, R. S. Carbon-Based Supercapacitors Produced by Activation of Graphene. *Science* **2011**, *332*, 1537–1541.
- (28) Pérez, C. R.; Yeon, S.-H.; Ségalini, J.; Presser, V.; Taberna, P.-L.; Simon, P.; Gogotsi, Y. Structure and Electrochemical Performance of Carbide-Derived Carbon Nanopowders. *Adv. Funct. Mater.* **2013**, *23*, 1081–1089.
- (29) Chmiola, J.; Yushin, G.; Gogotsi, Y.; Portet, C.; Simon, P.; Taberna, P. L. Anomalous Increase in Carbon Capacitance at Pore Sizes Less Than 1 Nanometer. *Science* **2006**, *313*, 1760–1763.
- (30) Gu, B.; Su, H.; Chu, X.; Wang, Q.; Huang, H.; He, J.; Wu, T.; Deng, W.; Zhang, H.; Yang, W. Rationally Assembled Porous Carbon Superstructures for Advanced Supercapacitors. *Chem. Eng. J.* **2019**, *361*, 1296–1303.
- (31) Liu, H.-J.; Wang, J.; Wang, C.-X.; Xia, Y.-Y. Ordered Hierarchical Mesoporous/Microporous Carbon Derived from Mesoporous Titanium-Carbide/Carbon Composites and its Electrochemical Performance in Supercapacitor. *Adv. Energy Mater.* **2011**, *1*, 1101–1108.
- (32) Zhao, M.-Q.; Ren, C. E.; Ling, Z.; Lukatskaya, M. R.; Zhang, C.; Van Aken, K. L.; Barsoum, M. W.; Gogotsi, Y. Flexible MXene/Carbon Nanotube Composite Paper with High Volumetric Capacitance. *Adv. Mater.* **2015**, *27*, 339–345.
- (33) Huang, H.; Su, H.; Zhang, H.; Xu, L.; Chu, X.; Hu, C.; Liu, H.; Chen, N.; Liu, F.; Deng, W.; Gu, B.; Zhang, H.; Yang, W. Extraordinary Areal and Volumetric Performance of Flexible Solid-State Micro-Supercapacitors Based on Highly Conductive Freestanding Ti<sub>3</sub>C<sub>2</sub>T<sub>x</sub> Films. *Adv. Electron. Mater.* **2018**, *4*, 1800179.
- (34) Lin, T.; Chen, I.-W.; Liu, F.; Yang, C.; Bi, H.; Xu, F.; Huang, F. Nitrogen-Doped Mesoporous Carbon of Extraordinary Capacitance for Electrochemical Energy Storage. *Science* **2015**, *350*, 1508–1513.
- (35) Liu, Y.; Shen, Y.; Sun, L.; Li, J.; Liu, C.; Ren, W.; Li, F.; Gao, L.; Chen, J.; Liu, F.; Sun, Y.; Tang, N.; Cheng, H.-M.; Du, Y. Elemental Superdoping of Graphene and Carbon Nanotubes. *Nat. Commun.* **2016**, *7*, 10921.
- (36) Zera, E.; Nickel, W.; Hao, G. P.; Vanzetti, L.; Kaskel, S.; Soraru, G. D. Nitrogen Doped Carbide Derived Carbon Aerogels by Chlorine Etching of a SiCN Aerogel. *J. Mater. Chem. A* **2016**, *4*, 4525–4533.
- (37) Ewert, J.-K.; Weingarh, D.; Denner, C.; Friedrich, M.; Zeiger, M.; Schreiber, A.; Jäckel, N.; Presser, V.; Kempe, R. Enhanced Capacitance of Nitrogen-Doped Hierarchically Porous Carbide-Derived Carbon in Matched Ionic Liquids. *J. Mater. Chem. A* **2015**, *3*, 18906–18912.
- (38) Chen, H.; Sun, F.; Wang, J.; Li, W.; Qiao, W.; Ling, L.; Long, D. Nitrogen Doping Effects on the Physical and Chemical Properties of Mesoporous Carbons. *J. Phys. Chem. C* **2013**, *117*, 8318–8328.
- (39) Pinkert, K.; Oschatz, M.; Borchardt, L.; Klose, M.; Zier, M.; Nickel, W.; Giebeler, L.; Oswald, S.; Kaskel, S.; Eckert, J. Role of Surface Functional Groups in Ordered Mesoporous Carbide-Derived Carbon/Ionic Liquid Electrolyte Double-Layer Capacitor Interfaces. *ACS Appl. Mater. Interfaces* **2014**, *6*, 2922–2928.
- (40) Zhao, Q.; Wang, X.; Liu, J.; Wang, H.; Zhang, Y.; Gao, J.; Liu, J.; Lu, Q. Surface Modification and Performance Enhancement of Carbon Derived from Chromium Carbide for Supercapacitor Applications. *J. Electrochem. Soc.* **2015**, *162*, A845–A851.
- (41) Liu, J.; Wang, X.; Lu, Q.; Yu, R.; Chen, M.; Cai, S.; Wang, X. Synthesis of Nitrogen and Sulfur Co-Doped Carbon Derived from Chromium Carbide for the High Performance Supercapacitor. *J. Electrochem. Soc.* **2016**, *163*, A2991–A2998.
- (42) Kou, Z.; Guo, B.; Zhao, Y.; Huang, S.; Meng, T.; Zhang, J.; Li, W.; Amiin, I. S.; Pu, Z.; Wang, M.; Jiang, M.; Liu, X.; Tang, Y.; Mu, S. Molybdenum Carbide-Derived Chlorine-Doped Ordered Mesoporous Carbon with Few-Layered Graphene Walls for Energy Storage Applications. *ACS Appl. Mater. Interfaces* **2017**, *9*, 3702–3712.
- (43) Su, H.; Huang, H.; Zhang, H.; Chu, X.; Zhang, B.; Gu, B.; Zheng, X.; Wu, S.; He, W.; Yan, C.; Chen, J.; Yang, W. In Situ Direct Method to Massively Prepare Hydrophilic Porous Carbide-Derived Carbons for High-Performance Supercapacitors. *ACS Appl. Energy Mater.* **2018**, *1*, 3544–3553.
- (44) Chmiola, J.; Largeot, C.; Taberna, P.-L.; Simon, P.; Gogotsi, Y. Desolvation of Ions in Subnanometer Pores and Its Effect on Capacitance and Double-Layer Theory. *Angew. Chem. Int. Ed.* **2008**, *47*, 3392–3395.
- (45) Lei, Z.; Zhang, J.; Zhang, L. L.; Kumar, N. A.; Zhao, X. S. Functionalization of Chemically Derived Graphene for Improving Its Electrocapacitive Energy Storage Properties. *Energy Environ. Sci.* **2016**, *9*, 1891–1930.
- (46) Dyatkin, B.; Zhang, Y.; Mamontov, E.; Kolesnikov, A. I.; Cheng, Y.; Meyer, H. M.; Cummings, P. T.; Gogotsi, Y. Influence of Surface Oxidation on Ion Dynamics and Capacitance in Porous and Nonporous Carbon Electrodes. *J. Phys. Chem. C* **2016**, *120*, 8730–8741.
- (47) Deng, Y.; Xie, Y.; Zou, K.; Ji, X. Review on Recent Advances in Nitrogen-Doped Carbons: Preparations and Applications in Supercapacitors. *J. Mater. Chem. A* **2016**, *4*, 1144–1173.
- (48) Pohl, M.; Kurig, H.; Tallo, I.; Jänes, A.; Lust, E. Novel Sol-Gel Synthesis Route of Carbide-Derived Carbon Composites for Very High Power Density Supercapacitors. *Chem. Eng. J.* **2017**, *320*, 576–587.
- (49) Borchardt, L.; Oschatz, M.; Kaskel, S. Tailoring Porosity in Carbon Materials for Supercapacitor Applications. *Mater. Horiz.* **2014**, *1*, 157–168.
- (50) Zou, X.; Ji, L.; Hsu, H.-Y.; Zheng, K.; Pang, Z.; Lu, X. Designed Synthesis of SiC Nanowire-Derived Carbon with Dual-Scale Nanostructures for Supercapacitor Applications. *J. Mater. Chem. A* **2018**, *6*, 12724–12732.
- (51) Presser, V.; Heon, M.; Gogotsi, Y. Carbide-Derived Carbons—From Porous Networks to Nanotubes and Graphene. *Adv. Funct. Mater.* **2011**, *21*, 810–833.
- (52) Lee, C.-W.; Yoon, S.-B.; Kim, H.-K.; Youn, H.-C.; Han, J.; Roh, K. C.; Kim, K.-B. A Two-Dimensional Highly Ordered Mesoporous Carbon/Graphene Nanocomposite for Electrochemical Double Layer Capacitors: Effects of Electrical and Ionic Conduction Pathways. *J. Mater. Chem. A* **2015**, *3*, 2314–2322.
- (53) Su, H.; Zhang, H.; Liu, F.; Chun, F.; Zhang, B.; Chu, X.; Huang, H.; Deng, W.; Gu, B.; Zhang, H.; Zheng, X.; Zhu, M.; Yang, W. High Power Supercapacitors Based on Hierarchically Porous

Sheet-Like Nanocarbons with Ionic Liquid Electrolytes. *Chem. Eng. J.* **2017**, *322*, 73–81.

(54) Li, W.; Zhang, F.; Dou, Y.; Wu, Z.; Liu, H.; Qian, X.; Gu, D.; Xia, Y.; Tu, B.; Zhao, D. A Self-Template Strategy for the Synthesis of Mesoporous Carbon Nanofibers as Advanced Supercapacitor Electrodes. *Adv. Energy Mater.* **2011**, *1*, 382–386.

(55) Fang, Y.; Luo, B.; Jia, Y.; Li, X.; Wang, B.; Song, Q.; Kang, F.; Zhi, L. Renewing Functionalized Graphene as Electrodes for High-Performance Supercapacitors. *Adv. Mater.* **2012**, *24*, 6348–6355.

(56) Park, S.-K.; Jin, A.; Yu, S.-H.; Ha, J.; Jang, B.; Bong, S.; Woo, S.; Sung, Y.-E.; Piao, Y. In Situ Hydrothermal Synthesis of Mn<sub>3</sub>O<sub>4</sub> Nanoparticles on Nitrogen-Doped Graphene as High-Performance Anode Materials for Lithium Ion Batteries. *Electrochim. Acta* **2014**, *120*, 452–459.

(57) Wang, J.; Ding, B.; Hao, X.; Xu, Y.; Wang, Y.; Shen, L.; Dou, H.; Zhang, X. A Modified Molten-Salt Method to Prepare Graphene Electrode with High Capacitance and Low Self-Discharge Rate. *Carbon* **2016**, *102*, 255–261.

(58) Arrigo, R.; Hävecker, M.; Wrabetz, S.; Blume, R.; Lerch, M.; McGregor, J.; Parrott, E. P. J.; Zeitler, J. A.; Gladden, L. F.; Knop-Gericke, A.; Schlögl, R.; Su, D. S. Tuning the Acid/Base Properties of Nanocarbons by Functionalization via Amination. *J. Am. Chem. Soc.* **2010**, *132*, 9616–9630.

(59) Oh, Y. J.; Yoo, J. J.; Kim, Y. I.; Yoon, J. K.; Yoon, H. N.; Kim, J.-H.; Park, S. B. Oxygen Functional Groups and Electrochemical Capacitive Behavior of Incompletely Reduced Graphene Oxides as a Thin-Film Electrode of Supercapacitor. *Electrochim. Acta* **2014**, *116*, 118–128.

(60) Zhang, W.; Xu, C.; Ma, C.; Li, G.; Wang, Y.; Zhang, K.; Li, F.; Liu, C.; Cheng, H.-M.; Du, Y.; Tang, N.; Ren, W. Nitrogen-Superdoped 3D Graphene Networks for High-Performance Supercapacitors. *Adv. Mater.* **2017**, *29*, 1701677.

(61) Zhang, Z.; Wang, L.; Li, Y.; Wang, Y.; Zhang, J.; Guan, G.; Pan, Z.; Zheng, G.; Peng, H. Nitrogen-Doped Core-Sheath Carbon Nanotube Array for Highly Stretchable Supercapacitor. *Adv. Energy Mater.* **2017**, *7*, 1601814.

(62) Wang, D.-W.; Li, F.; Yin, L.-C.; Lu, X.; Chen, Z.-G.; Gentle, I. R.; Lu, G. Q.; Cheng, H.-M. Nitrogen-Doped Carbon Monolith for Alkaline Supercapacitors and Understanding Nitrogen-Induced Redox Transitions. *Chem. Eur. J.* **2012**, *18*, 5345–5351.

(63) Graupner, R.; Abraham, J.; Vencelová, A.; Seyller, T.; Hennrich, F.; Kappes, M. M.; Hirsch, A.; Ley, L. Doping of Single-Walled Carbon Nanotube Bundles by Brønsted Acids. *Phys. Chem. Chem. Phys.* **2003**, *5*, 5472–5476.

(64) Li, X.; Lau, S. P.; Tang, L.; Ji, R.; Yang, P. Multicolour Light Emission from Chlorine-Doped Graphene Quantum Dots. *J. Mater. Chem. C* **2013**, *1*, 7308–7313.

(65) Su, C.; Pei, C.; Wu, B.; Qian, J.; Tan, Y. Highly Doped Carbon Nanobelts with Ultrahigh Nitrogen Content as High-Performance Supercapacitor Materials. *Small* **2017**, *13*, 1700834.

(66) Kant, R.; Singh, M. B. Theory of the Electrochemical Impedance of Mesostructured Electrodes Embedded with Heterogeneous Micropores. *J. Phys. Chem. C* **2017**, *121*, 7164–7174.

(67) Wang, J.; Polleux, J.; Lim, J.; Dunn, B. Pseudocapacitive Contributions to Electrochemical Energy Storage in TiO<sub>2</sub> (Anatase) Nanoparticles. *J. Phys. Chem. C* **2007**, *111*, 14925–14931.

(68) Kim, H.-S.; Cook, J. B.; Lin, H.; Ko, J. S.; Tolbert, S. H.; Ozolins, V.; Dunn, B. Oxygen Vacancies Enhance Pseudocapacitive Charge Storage Properties of MoO<sub>3-x</sub>. *Nat. Mater.* **2017**, *16*, 454–460.

(69) Lee, Y.-H.; Chang, K.-H.; Hu, C.-C. Differentiate the Pseudocapacitance and Double-Layer Capacitance Contributions for Nitrogen-Doped Reduced Graphene Oxide in Acidic and Alkaline Electrolytes. *J. Power Sources* **2013**, *227*, 300–308.

(70) Lee, J.-S. M.; Briggs, M. E.; Hu, C.-C.; Cooper, A. I. Controlling Electric Double-Layer Capacitance and Pseudocapacitance in Heteroatom-Doped Carbons Derived from Hypercrosslinked Microporous Polymers. *Nano Energy* **2018**, *46*, 277–289.

(71) Kant, R.; Singh, M. B. Generalization of the Gouy-Chapman-Stern Model of an Electric Double Layer for a Morphologically

Complex Electrode: Deterministic and Stochastic Morphologies. *Phys. Rev. E* **2013**, *88*, No. 052303.